Available online at www.synsint.com

Synthesis and Sintering

ISSN 2564-0186 (Print), **ISSN** 2564-0194 (Online)

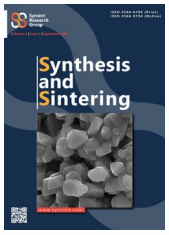

Research article

Microstructure and electrical properties of spark plasma sintered $Li_{1+x}Ce_xZr_{2-x}(PO_4)_3$ as solid electrolyte for lithium-ion batteries

Zahra Khakpour [a,*], **Saeed Sedaghat** [a], **Mohammad Farvizi** [b], **Nima Naderi** [c], **Abouzar Massoudi** [c]

[a] *Ceramic Department, Materials and Energy Research Center (MERC), Karaj, Iran*
[b] *Department of Materials Engineering, Faculty of Mechanical Engineering, University of Tabriz, Tabriz 51666-16471, Iran*
[c] *Department of Semiconductors, Materials and Energy Research Center (MERC), Karaj, Iran*

A B S T R A C T

In this study, the microstructural and electrical characteristics of spark plasma sintered $Li_{1+x}Ce_xZr_{2-x}(PO_4)_3$ solid electrolytes were investigated, specifically underlining the impacts of Ce substitution on their performance as Li-ion battery electrolytes. Samples with varying amounts of Ce (x = 0.1, 0.2, and 0.3) were synthesized via the conventional solid-state reaction method. The densified samples were systematically characterized using advanced techniques, including X-ray diffraction (XRD) for phase detection, field emission scanning electron microscopy (FESEM) for microstructural analysis, and energy-dispersive X-ray spectroscopy (EDS) for elemental analysis. A significant improvement in densification and a subsequent reduction in porosity were observed in the SPSed samples, with the LZPC3 sample achieving a high relative density of 92.08%. The XRD and EDS analyses confirmed the formation of the main NASICON phase along with a Ce-rich secondary phase that segregated during the SPS process. Crucially, the Nyquist plot analysis revealed that Ce substitution did not hinder Li^+ ion transport; instead, the overall ionic conductivity of the LZPC3 sample was substantially enhanced compared to the undoped LZP sample. This positive outcome is attributed to the aliovalent substitution (Ce^{3+} for Zr^{4+}), effectively increasing the concentration of mobile charge carriers. The high densification and significant enhancement in ionic conductivity achieved through Ce doping and SPS processing demonstrate the potential of this composition for advanced solid-state electrolyte applications.

KEYWORDS

$Li_{1+x}Ce_xZr_{2-x}(PO_4)_3$
Ionic conductivity
Spark plasma sintering
Cerium substitution
Microstructural analysis
Solid electrolyte

OPEN ACCESS

1. Introduction

In recent decades, lithium-ion batteries (LIBs) have gained significant commercial and scientific attention among the different metal-ion batteries. LIBs possess several industrial devices and portable electronic applications, including laptops, mobiles, electric vehicles, and energy grids [1]. Much effort has been made to improve the performance of the new generation of LIBs, like improvement of their power and energy densities, enhancing their cost-effectiveness, and, more importantly, enhancing their safety for large-scale applications [2, 3].

* Corresponding author. *E-mail address:* z.khakpour@merc.ac.ir (Z. Khakpour)
Received 26 June 2025; Received in revised form 30 September 2025; Accepted 30 September 2025.

https://doi.org/10.53063/synsint.2025.53293

Different safety challenges like leakage, restricted operational temperature range, and flammability can be minimized by developing all-solid-state batteries (ASSBs), in which the liquid electrolyte used in conventional batteries is replaced with a solid electrolyte. Additionally, using a solid electrolyte in the battery can contribute to higher energy density and a longer cycle life [4]. Recently, several studies have focused on the transport and structural behavior of a broad variety of inorganic solid electrolytes. Nevertheless, researchers still try to attain an optimal and affordable solid electrolyte that offers ionic conductivity comparable to that of liquid electrolytes, along with good electrochemical, mechanical, and thermal stability, and low resistance at the electrode interface for commercial applications [5, 6].

NASICON-type solid electrolytes (Li-ion conducting $Na_3Zr_2Si_2PO_{12}$) are known for their decent ionic conductivity, strong chemical stability, and relatively low interfacial resistance compared to other inorganic solid electrolytes, such as sulfides, oxides, and hydrides [7–9]. $LiZr_2(PO_4)_3$ (LZP) is a NASICON-type solid electrolyte, fitting the general formula $LiX_2(PO_4)_3$, where X can be Ge, Ti, or Zr. The LZP structure features a robust framework composed of corner-sharing PO_4 tetrahedra and ZrO_6 octahedra, creating a 3D network of interstitial tunnels that facilitate the easy diffusion of Li-ions [10]. While $LiGe_2(PO_4)_3$ and $LiTi_2(PO_4)_3$ often present greater ionic conductivity values, LZP demonstrates excellent chemical stability when in contact with Li metal, which can be attributed to the stability provided by the Zr^{4+} ion [11].

The LZP compound has complicated polymorphism according to the starting compounds and synthesis conditions utilized for the fabrication of the material [12–14]. LZP crystallized in the rhombohedral phase demonstrates the highest ionic conductivity owing to its advantageous crystal arrangement, which facilitates the rapid diffusion of Li-ions. Recent research works indicate that by optimizing the sintering parameters, Zr precursor, and doping methods, LZP can be synthesized to crystallize in the rhombohedral phase at room temperature [15–17].

In the present study, $Li_{1+x}Ce_xZr_{2-x}(PO_4)_3$ solid electrolytes with different amounts of Ce (x = 0.1, 0.2, and 0.3) are sintered by both SPS and conventional methods. The primary goal is to study the effect of the aliovalent Ce^{3+} substitution for Zr^{4+} on the densification, phase stability, and, most importantly, the ionic conductivity of this NASICON material.

2. Experimental

2.1. Materials and processing

The solid electrolyte powders with the nominal formula $Li_{1+x}Ce_xZr_{2-x}(PO_4)_3$ were synthesized using a conventional solid-state reaction method. The chosen substitution levels for the Ce^{3+} ion were x = 0.1, 0.2, and 0.3. An undoped $LiZr_2(PO_4)_3$ sample (x = 0) was also prepared for comparison. The nominal compositions and corresponding sample codes are listed in Table 1. The starting materials used were high-purity zirconium dioxide (ZrO_2), lithium carbonate (Li_2CO_3), ammonium dihydrogen phosphate ($(NH_4)_2HPO_4$), and cerium(III) nitrate hexahydrate ($Ce(NO_3)_3.6H_2O$). The required stoichiometric quantities of these raw materials were accurately weighed for each composition, as detailed in Table 2, and subsequently mixed thoroughly in an agate mortar to ensure maximum homogeneity.

Table 1. Nominal compositions and corresponding sample codes for the $Li_{1+x}Ce_xZr_{2-x}(PO_4)_3$ solid electrolytes.

Sample code	x	Composition
LZP	0.0	$LiZr_2(PO_4)_3$
LZPC1	0.1	$Li_{1.1}Ce_{0.1}Zr_{1.9}(PO_4)_3$
LZPC2	0.2	$Li_{1.2}Ce_{0.2}Zr_{1.8}(PO_4)_3$
LZPC3	0.3	$Li_{1.3}Ce_{0.3}Zr_{1.7}(PO_4)_3$

After weighing all components, the $Ce(NO_3)_3.6H_2O$, based on the target compositions, was introduced into the corresponding powder mixtures. Each powder batch was then homogenized for 20 min using a tubular mixer. To eliminate any adsorbed moisture from the initial mixing, the prepared mixtures were transferred to 100 cc alumina crucibles and placed in an oven at 110 °C for 4 hours for dehydration. Following this drying step, the powder mixtures were subjected to dry milling using a planetary ball mill for 1 hour at a rotation speed of 220 rpm, utilizing zirconia cups and balls. Subsequently, the four distinct powder mixtures were poured into four separate alumina crucibles. These crucibles were then placed inside a box furnace with an air atmosphere to complete the material synthesis. The detailed heating schedule employed for the synthesis process is shown in Fig. 1. Following the completion of the synthesis heating program, the furnace was turned off, allowing the internal temperature to gradually decrease. This slow cooling process served to slowly anneal the powders back to ambient conditions. The synthesized powders were then removed. It was observed that due to the phosphate nature of the compounds, the powders significantly expanded during the high-temperature treatment, resulting in porous, puffy structures. This expansion is likely attributed to the vigorous release of gases during the solid-state reaction.

After being carefully separated from the alumina crucibles, the synthesized $Li_{1+x}Ce_xZr_{2-x}(PO_4)_3$ powders were subjected to a refining step. They were dry milled in a planetary ball mill for 1 hour at a rotation speed of 300 rpm to break down agglomerates. Subsequently, the powders were passed through a 400-mesh sieve to ensure a narrow and uniform particle size distribution. The final powders, with particle sizes confirmed to be less than 37 μm, were then ready for shaping and further analysis.

Cylindrical pellets were fabricated from the refined powders of each composition using a uniaxial hydraulic press. The pressing process involved two stages of pressure application: an initial pressure of 10 MPa, followed by a final, higher pressure ranging from 80 to 100 MPa. The resulting pressed pellets had standardized dimensions, typically featuring a diameter of 13 mm and a thickness between 8 and 9 mm. An image illustrating three of these prepared samples is presented in Fig. 2.

For densification, the prepared cylindrical-shaped samples were placed in alumina crucibles and sintered in a box furnace (Amalgam model,

Table 2. Weight percentages of the raw materials used for the synthesis of the undoped $LiZr_2(PO_4)_3$ (LZP) reference sample.

Raw materials	ZrO_2	Li_2CO_3	$(NH_4)_2HPO_4$
wt%	36.27	5.44	58.29

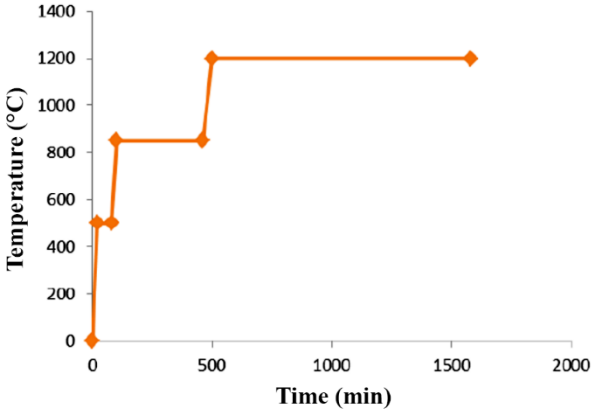

Fig. 1. Optimized heating program for the synthesis of the powder mixtures [16].

Iran). The sintering was carried out using the muffle method in a powder bed. This technique was employed to minimize both potential contamination and the loss of volatile species (primarily lithium) during the high-temperature treatment. The specific heating program for the sintering step is illustrated in Fig. 3.

To manufacture high-density samples using the SPS method, an initial assessment based on previous studies suggested that the x = 0.3 composition, designated as LZPC3, would likely yield optimal densification and electrical properties. Considering the intensive resource requirements and time investment associated with the SPS technique, only the undoped reference LZP (x=0) and the highly doped LZPC3 (x=0.3) compositions were selected for SPS treatment. A photograph of the SPS apparatus used is shown in Fig. 4.

The LZP and LZPC3 powders were carefully loaded into a graphite mold. The interior of the mold was lined with thin, flexible graphite foil. This lining served the dual purpose of preventing any potential sticking of the ceramic powders to the mold walls and minimizing undesirable chemical reactions between the graphite components and the powders during the high-temperature process. The SPS procedure was carried out at a temperature of 1200 °C for a dwell time of 20 min. This heating cycle was performed under a uniaxial mechanical pressure of 30 MPa applied throughout the process and conducted in a vacuum atmosphere.

Fig. 2. Image of three representative cylindrical green body pellets prepared by uniaxial hydraulic pressing before sintering.

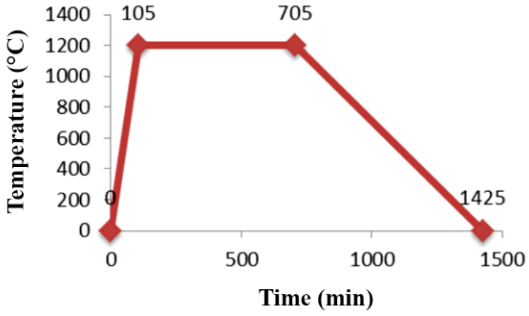

Fig. 3. Temperature profile used for the conventional sintering of the pressed green body pellets [16].

2.2. Characterization

The densities of the synthesized powders were determined using a glass pycnometer method, in accordance with the EN 1097-6 standard. The bulk densities of the densified samples (both conventionally sintered and SPS-processed) were measured using the Archimedes method. The relative densities were subsequently calculated by dividing the measured bulk densities by their theoretical density values.

The crystalline phases present in both the synthesized powders and the densified specimens were identified through X-ray diffraction (XRD) analysis, carried out using a Philips PW3710 diffractometer. The morphological characteristics of the synthesized powders and the microstructure of the dense specimens were investigated using field emission scanning electron microscopy (FESEM) (Tescan S8000). Further elemental composition analysis was performed using energy-dispersive X-ray spectroscopy (EDS).

Ionic conductivity measurements were performed on the polished samples using an impedance analyzer (Autolab-PGstate30). Before measurement, both sides of the samples were coated with a thin layer of gold (Au) via magnetron sputtering to ensure high electrical conductivity and excellent contact quality between the sample and the electrodes.

Fig. 4. The SPS apparatus used for the densification of pellets.

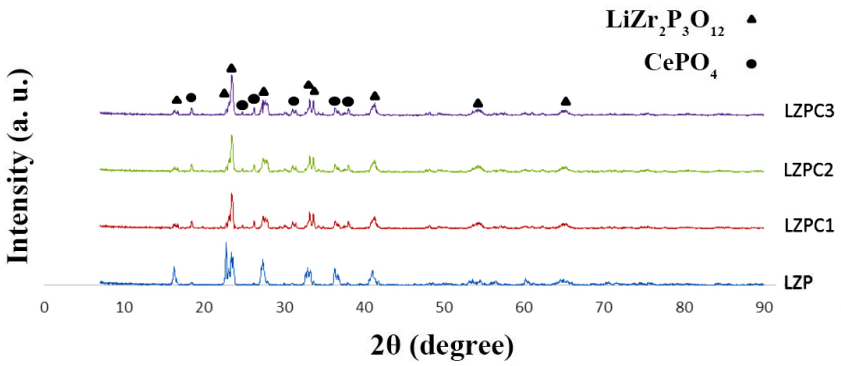

Fig. 5. XRD patterns of the synthesized $Li_{1+x}Ce_xZr_{2-x}(PO_4)_3$ powders for various Ce substitution levels.

3. Results and discussion

3.1. Synthesized powder samples

The XRD analysis results for the synthesized $Li_{1+x}Ce_xZr_{2-x}(PO_4)_3$ powders are illustrated in Fig. 5. As evidenced by the sharp and strong intensity of the peaks in Fig. 5, the synthesized materials are fully crystalline, indicating the successful formation of the desired crystalline structure and the absence of any amorphous phases. Given that the synthesis procedure was conducted at a temperature of 1200 °C, the resulting compositions are expected to exhibit a mixture of both the rhombohedral ($R\bar{3}c$) and monoclinic (C2/c) crystal structures [18]. It is worth noting that the rhombohedral structure (typically associated with NASICON-type electrolytes) is highly desirable due to its superior ionic conductivity.

Focusing on the undoped LZP sample (x=0), the diffraction peaks for $LiZr_2(PO_4)_3$ show good alignment with the reference data (JCPDS card no. 00-33-777). However, a slight shift in the peak positions towards higher angles (2θ) is noticeable. This slight shift may be attributed to the interdiffusion of elements from the raw materials into the lattice during synthesis, potentially causing a minor change in the unit cell volume and lattice spacing d, in accordance with Bragg's Law ($\lambda = 2d \sin\theta$).

As displayed in Fig. 5, peaks corresponding to cerium phosphate ($CePO_4$), a secondary phase, have emerged in the XRD patterns of the Ce-doped samples (LZPC1, LZPC2, LZPC3). As the Ce content increases in the compositions, the intensity of the peaks related to the main rhombohedral structure also increases. However, since the substitution levels (x = 0.1 to 0.3) are relatively small, this intensity enhancement is not pronounced and is primarily detectable in the principal diffraction peaks. Furthermore, a small amount of unreacted ZrO_2 has also been identified in the synthesized powders.

The morphology of the synthesized powders, LZP and LZPC3, was investigated using FESEM. The resulting images are presented in Fig. 6. Analysis of the FESEM micrographs reveals that both the undoped (LZP) and the Ce-doped (LZPC3) powders consist of highly irregular and angular particles. These particles lack any uniform shape, which is characteristic of materials synthesized by the conventional solid-state reaction route. The particle sizes are not uniform, spanning a wide range from sub-micron to the lower micron range, confirming that

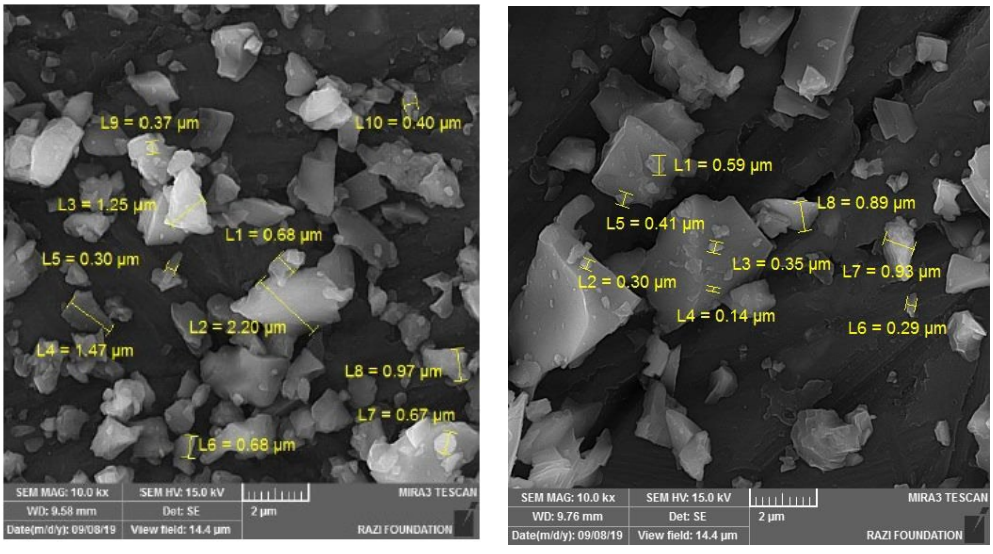

Fig. 6. FESEM images of the synthesized a) LZP [16] and b) LZPC3 powders.

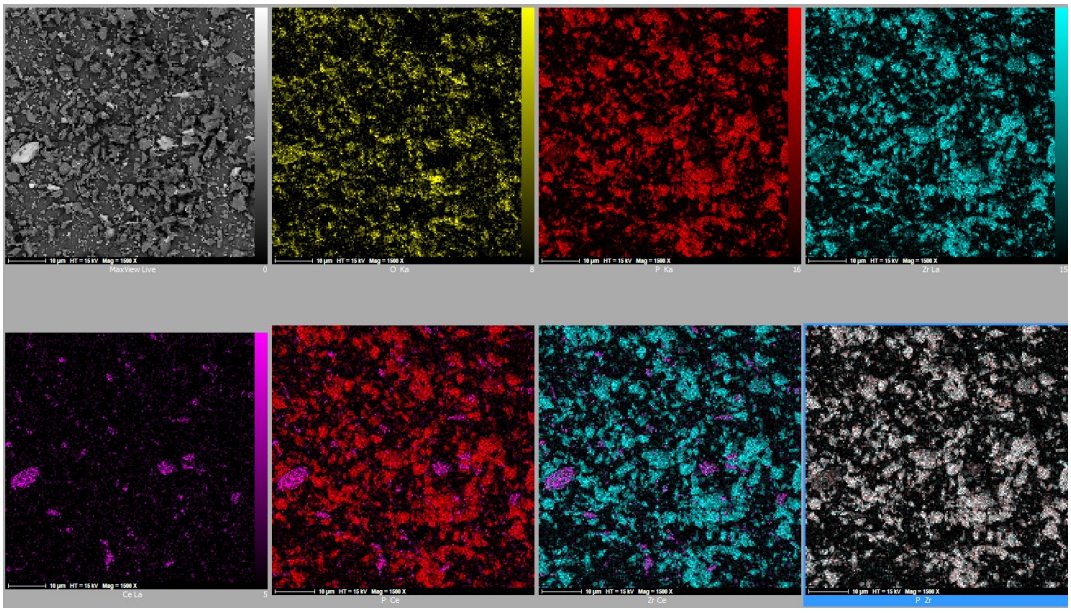

Fig. 7. EDS mapping of the synthesized LZPC3 powder.

particle refinement through the post-synthesis ball milling process was partially successful.

Element distribution across the surface of the LZPC3 powder was analyzed using the SE detector coupled with the Energy-Dispersive X-ray Spectroscopy (EDS) system. The elemental maps, which illustrate the distribution of constituent elements, are presented in Fig. 7. A key observation from these maps is the homogeneous overlay in the distribution of Zr and P elements. This overlapping distribution is crucial as it indicates the close spatial arrangement of ZrO_6 octahedra and PO_4 tetrahedra within the structure. This finding is consistent with the desired rhombohedral (NASICON) structure of the synthesized powder. However, the maps also reveal the presence of Ce with a tendency for localized clusters or regions of increased aggregation in certain spots. This clustering suggests the existence of an unwanted secondary phase, specifically cerium phosphate ($CePO_4$), within the LZPC3 powder matrix. This observation further supports the XRD findings regarding the presence of a minor Ce-based impurity phase.

The densities of the synthesized powders, measured using a pycnometer, are listed in Table 3. As clearly observed from the data, the powder densities consistently decrease as the content of the Ce additive increases. The density drops from 2.6634 g/cm^3 for the undoped LZP sample to 2.6111 g/cm^3 for the LZPC3 composition.

Table 3. Measured densities of the synthesized $Li_{1+x}Ce_xZr_{2-x}(PO_4)_3$ powders.

Sample code	Density (g/cm^3)
LZP	2.6634
LZPC1	2.6233
LZPC2	2.6214
LZPC3	2.6111

This systematic decrease in powder density can be explained by considering the effect of substituting Ce^{3+} for Zr^{4+} within the NASICON lattice. This substitution process simultaneously influences two main factors, as detailed in Table 4:

1- Atomic weight: The substitution of Zr (atomic weight: 91.2 g/mol) with Ce (atomic weight: 140.1 g/mol) results in an overall increase in the atomic weight of the unit cell.

2- Unit cell volume: the atomic radius of Ce (181.8 nm) is significantly larger than that of Zr (158 nm). Consequently, the incorporation of the larger Ce ion causes an expansion, or increase, in the volume of the unit cell.

In the case of Ce substitution, the expansion of the unit cell volume due to the larger Ce radius has a more substantial effect than the increase in the overall atomic weight. Since density is mass divided by volume, the dominant increase in unit cell volume leads to the observed reduction in the overall density of the powders as the additive content increases.

3.2. Sintered samples

The densification behavior of the LZP sample during the SPS process is analyzed by plotting the displacement (reduction in sample thickness) versus sintering time. This diagram is illustrated in Fig. 8. The sample was processed at a maximum temperature of 1200 °C for a dwell time of 20 min at the peak temperature. The displacement-time curve exhibits several distinct stages.

Table 4. Atomic characteristics of zirconium and cerium.

Element	Atomic weight (g/mol)	Atomic radius (nm)
Zr	91.2 [19]	158 [20]
Ce	140.1 [21]	181.8 [22]

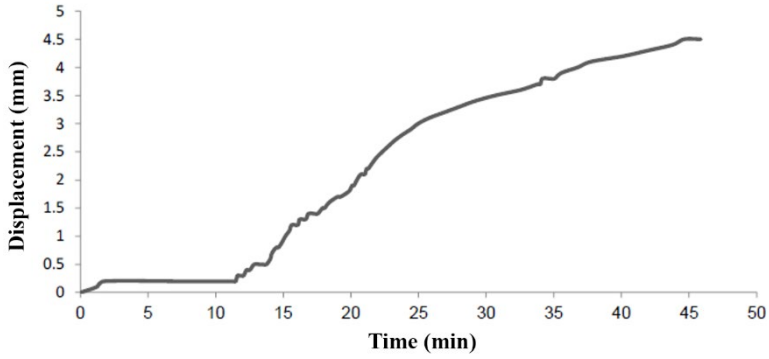

Fig. 8. The displacement-time diagram of SPSed LZP [16].

An initial, small reduction in sample thickness is observed within the first two minutes of the process. Since the electric current and resulting Joule heating have not yet fully commenced in this very early stage, this initial displacement is primarily attributed to the direct application of the mechanical pressure (30 MPa) on the powder bed.

Afterward, the thickness of the sample remains largely constant up to the 12th minute, indicating a pre-sintering stabilization period. Starting around the 12th minute, a sharp and significant reduction in sample thickness is initiated. This marks the onset of the main densification phase. As the electric current increases, the primary Joule heating mechanism activates within the powder particles. This intense heating facilitates particle rearrangement, which fills the existing porosity and dramatically reduces the sample thickness.

Concurrently, based on the ohmic heating mechanism, the sparks generated between particles and the subsequent plasma formation contribute significantly to neck formation between adjacent grains. This rapid localized heating can momentarily raise the temperature at the grain interfaces, leading to surface melting and accelerating necking [23]. After this initial rapid phase, the rate of densification slows down considerably (around the 35th minute). At this point, the ohmic mechanism responsible for spark generation diminishes or becomes disabled, leaving the Joule heating as the dominant mechanism to continue densification, which is critical for achieving high final density. The final stage of densification is linked to grain growth, which is typically considered negligible in the context of total densification [24, 25].

Table 5 lists the measured bulk density, calculated relative density, and total porosity for the cold-pressed green bodies and the densified SPSed samples. The bulk density measurements were performed using Archimedes' method. Comparing the cold-pressed samples reveals a trend of increasing relative density as the amount of Ce additive increases. The relative density improves from 76.11% for the undoped LZP sample to 78.52% for the LZPC3 composition. This enhanced densification suggests that the incorporation of the Ce additive facilitates better packing and reduced porosity in the green body structure.

The use of the SPS technique significantly boosts the densification performance compared to simple cold pressing. As observed in Table 5, the SPSed samples possess substantially higher relative densities and lower total porosities. Specifically, the relative density of the LZP sample increases from 76.11% (pressed) to 86.47% (SPSed). The maximum densification is achieved with the Ce-doped LZPC3 sample, reaching an impressive relative density of 92.08% and a total porosity of only 7.92% after the SPS process. This high density confirms the effectiveness of the SPS method combined with the beneficial presence of the Ce additive.

The improvement in the final densification for Ce-doped samples, particularly under SPS, can be attributed to two main factors. First, the substitution of Zr^{4+} by the larger Ce^{3+} ion may lead to the local formation of a minor glassy phase during the high-temperature processing. The presence of this glassy phase can significantly enhance the sinterability of the powders by promoting liquid-phase sintering mechanisms. Second, the higher atomic weight of Ce (compared to Zr) contributes to an overall increase in the specific weight of the final densified material, which mathematically aids in achieving a higher bulk density.

Fig. 9 presents the results of the XRD analysis, which were used to identify the phase composition of the SPSed samples. Fig. 9a shows the

Table 5. Bulk density, relative density, and total porosity of the cold-pressed and SPSed samples.

Sample	Bulk density (g/cm^3)	Relative density (%)	Total porosity (%)
LZP (Pressed)	2.0271	76.11	23.89
LZPC1 (Pressed)	2.0275	77.29	22.71
LZPC2 (Pressed)	2.0410	77.86	22.14
LZPC3 (Pressed)	2.0502	78.52	21.48
LZP (SPSed)	2.3030	86.47	13.53
LZPC3 (SPSed)	2.4043	92.08	7.92

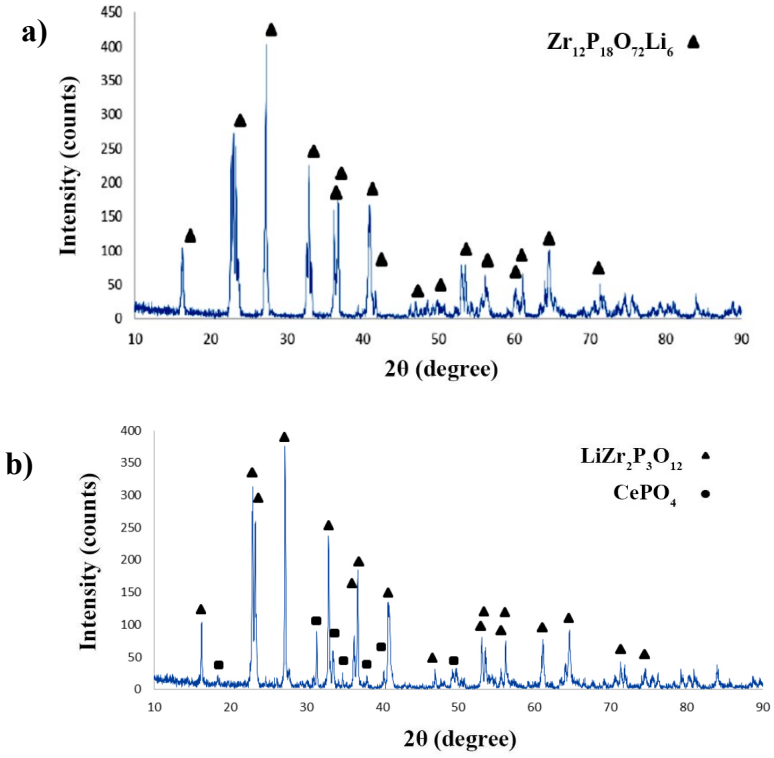

Fig. 9. XRD results of SPSed a) LZP [16] and b) LZPC3.

pattern for the undoped LZP sample, and Fig. 9b displays the pattern for the LZPC3 sample. As expected, the intensity of the XRD peaks increased significantly in both SPSed samples compared to the synthesized powders (Fig. 5). This increase in intensity is a direct result of the high-temperature and high-pressure treatment during SPS, which leads to greater crystalline perfection, ordering, and alignment of the grains.

In the additive-free LZP sample, the diffraction pattern confirms the existence of the pure NASICON-type phase, identified as $LiZr_2(PO_4)_3$, which possesses the highly desirable rhombohedral structure ($R\bar{3}c$), consistent with reference JCPDS card no. 96-400-0263. For the Ce-doped LZPC3 sample, the main rhombohedral NASICON phase is also predominant. However, in addition to the main phase, distinct additional peaks corresponding to a new secondary phase ($CePO_4$) have appeared. These peaks are marked by the black square symbol in the LZPC3 pattern. This new phase formed during the high-pressure and high-temperature SPS process. This result is significant because the minor cerium phosphate impurity observed in the powder stage (Fig. 5) appears to have reacted or transformed, leading to the formation of this distinct secondary phase during densification. The presence of this new minor phase in the LZPC3 sample highlights the chemical reactivity of the cerium substitution at the extreme conditions of SPS. This phase could potentially impact the grain boundary structure and, consequently, the overall ionic conductivity.

The FESEM images showing the fractured surfaces of the SPSed samples are presented in Fig. 10. These micrographs provide insight into the effectiveness of the SPS process and the impact of the Ce additive on the final densified structure. Fig. 10a shows the microstructure of the undoped LZP sample. The image reveals noticeable residual porosity, which aligns well with its calculated relative density of 86.47% (as listed in Table 5). Despite the presence of porosity, good necking and particle-to-particle connection are evident, confirming that the SPS process successfully initiated sintering. However, the porosity was not fully eliminated, likely due to the selection of a synthesis temperature (or dwell time) that was insufficient for the complete densification of the pure LZP composition. The grains in this sample generally appear distinct, with clear boundaries.

In contrast, Fig. 10b displays the microstructure of the LZPC3 sample. The addition of Ce led to a significant improvement in densification, which is consistent with its high relative density of 92.08%. The micrograph shows a much more integrated microstructure where porosity is substantially reduced, and the grains are in full contact with one another. This observation indicates improved sinterability and confirms the positive effect of the Ce additive on the densification process. Furthermore, a comparative analysis suggests that grain growth has occurred in the LZPC3 sample due to the incorporation of the Ce additive and the high-energy SPS treatment. The grains in the LZPC3 sample appear larger and more interlocked than those in the pure LZP sample. This increased grain size is attributed to the presence of Ce, which may enhance mass transport mechanisms during sintering.

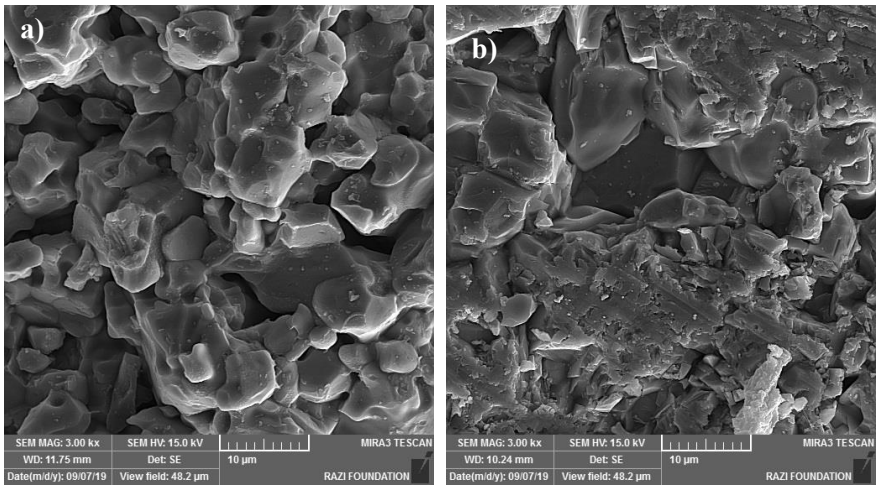

Fig. 10. FESEM images of the fractured surfaces of SPSed samples a) LZP [16] and b) LZPC3.

The backscattered FESEM image and the corresponding EDS analysis results for the SPSed LZPC3 sample are presented in Fig. 11. The backscattered image highlights distinct compositional differences due to phase segregation, as shown by the color contrast between point A and point B. Point A appears brighter due to a higher concentration of heavier elements, while point B has a darker contrast. The quantitative EDS data in the accompanying table confirms this difference. Point A exhibits a significantly higher concentration of Ce (44.74 wt%) and

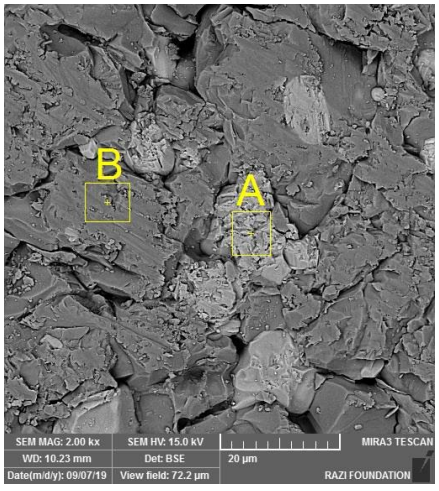

	POINT A		POINT B	
ELT	W%	A%	W%	A%
C	5.21	22.28	10.07	29.99
O	13.48	43.29	17.83	39.87
P	6.08	10.08	13.29	15.34
Zr	0.00	0.00	19.19	7.53
Ce	44.74	16.40	1.01	0.26
Au	30.50	7.95	38.60	7.01
+	100.00	100.00	100.00	100.00

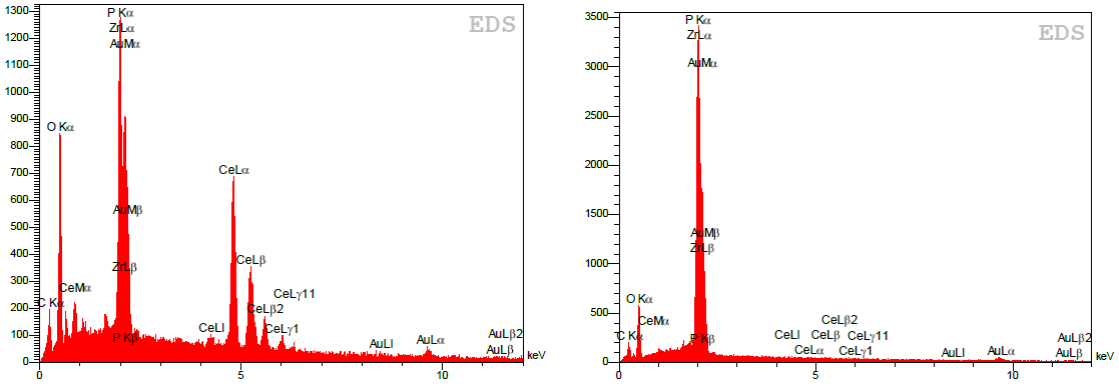

Fig. 11. The backscattered FESEM image and EDS analysis of the SPSed LZPC3 sample.

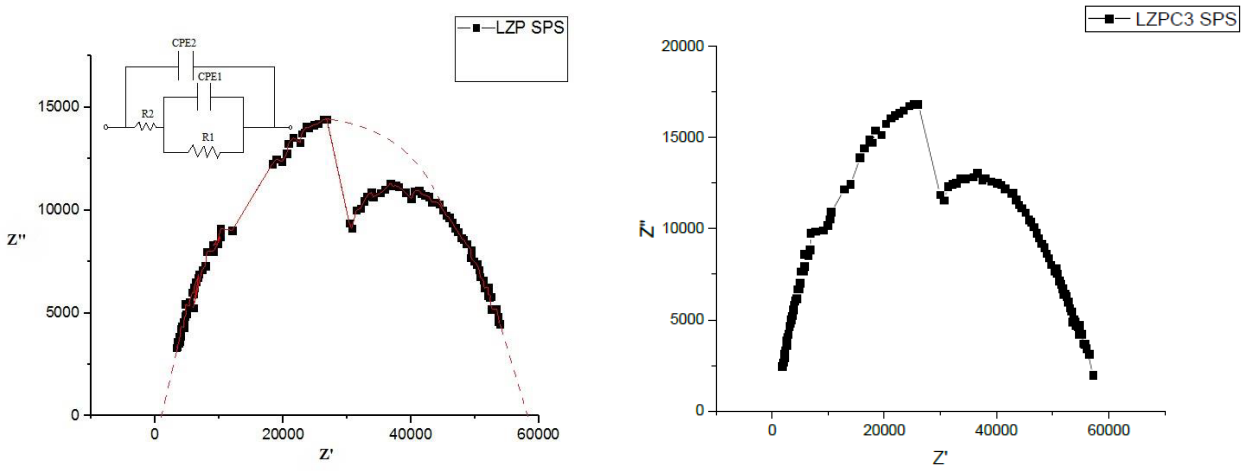

Fig. 12. Nyquist plots of SPSed LZP [16] and LZPC3.

virtually no Zr (0.00 wt%). Conversely, point B contains a high amount of zirconium (19.19 wt%) and only a very low concentration of cerium (1.01 wt%). Based on these elemental concentrations, it can be concluded that:

Point A (bright area) is an area of Ce enrichment and represents the secondary phase formed during the SPS process, which is likely cerium phosphate ($CePO_4$) or a cerium-rich compound. This segregation is consistent with the presence of the minor secondary phase observed in the XRD pattern (Fig. 9). Point B (darker area) represents the main $LiZr_2(PO_4)_3$ NASICON phase, characterized by its high zirconium content. The high concentration of the secondary phase at point A suggests that, despite the high mechanical pressure and rapid heating rate of the SPS process, the Ce-based impurity did not fully react or dissolve into the NASICON lattice. Instead, it segregated to the grain boundaries or specific locations during the densification process. A note regarding the quantitative analysis is necessary: due to the significant overlap between the energy peaks of P, Zr, and the gold (Au) coating applied to the sample for conductivity measurements, accurately determining the precise percentage of these elements using EDS is inherently difficult.

Some samples were tested using an impedance analyzer to determine their total electrical conductivity through Nyquist plot analysis. The resulting data were processed using ZView software, and the ionic resistances were calculated. Fig. 12 presents the Nyquist plots for the SPSed LZP and LZPC3 samples. Typically, the spectrum for a solid electrolyte consists of two semicircles and a low-frequency spike. The semicircles correspond to the intrinsic resistance of the material. The first semicircle (at higher frequencies) is associated with the intrinsic response of the grain (R_g), while the second semicircle or an additional arc is typically attributed to the grain boundary resistance (R_{gb}). The low-frequency line (not fully visible here but implied) may indicate a diffusion process, often associated with the movement of Li^+ ions across grain boundaries.

The Nyquist plot for the LZP sample (Fig. 12a) clearly shows two resolved semicircles. The first, smaller semicircle corresponds to the ionic conductivity within the grains. The second, larger semicircle or arc indicates the grain boundary resistance. For many ceramic electrolytes, the grain boundaries exhibit significantly higher resistivity than the grain interiors. The equivalent circuit used for fitting these data, shown as an inset, typically models the grain and grain boundary resistances using R-CPE (Resistor-Constant Phase Element) elements.

Fig. 12b shows the Nyquist plot for the LZPC3 sample. Visual inspection reveals that the overall size of the semicircles for LZPC3 is significantly smaller than that of the undoped LZP sample. This reduction in the total impedance ($Z_{total} = R_g + R_{gb}$) indicates that the addition of Ce and its subsequent high-density processing via SPS has substantially increased the overall ionic conductivity of the material. The improvement in conductivity suggests that the substitution of Ce did not hinder the movement of Li^+ ions; rather, the aliovalent substitution (Ce^{3+} for Zr^{4+}) effectively increased the concentration of mobile Li^+ carriers, leading to lower impedance. While the EDS analysis confirmed phase segregation of a Ce-rich secondary phase (Fig. 11), the overall beneficial effect of the Ce substitution on the bulk and grain boundary resistance appears to be dominant.

This result contrasts with the findings for the Gd-doped system, where Gd substitution appeared to increase the overall impedance [16]. In the Ce system, the Ce additive successfully achieved a superior trade-off between structural integrity (higher density, 92.08%) and enhanced ionic transport, making Ce a more effective dopant for LZP electrolytes under SPS conditions.

4. Conclusions

This study successfully synthesized and characterized $Li_{1+x}Ce_xZr_{2-x}(PO_4)_3$ solid electrolytes, providing valuable insights into the impact of Ce substitution on their structural and electrical properties. The solid-state reaction method successfully produced the primary NASICON phase, although minor Ce-rich secondary phases were detected, particularly in the highly doped LZPC3 powder. The comparative analysis of SPS and cold pressing confirmed that SPS significantly enhances densification, reducing porosity and leading to superior structural integrity. The optimum composition, LZPC3 (x = 0.3), achieved a maximum relative density of 92.08% after SPS. Crucially, the incorporation of Ce into the NASICON structure, facilitated by SPS, resulted in a substantial increase in overall ionic conductivity compared to the undoped LZP sample. This enhancement

is attributed to the aliovalent substitution of Ce^{3+} for Zr^{4+}, which effectively increases the concentration of mobile Li^{+} charge carriers within the lattice. The Ce substitution proved to be highly effective in achieving a favorable trade-off between maximizing structural density and enhancing ionic transport. Overall, these findings underscore the potential of using Ce doping in conjunction with the SPS technique to tailor NASICON electrolytes for more efficient and reliable all-solid-state battery applications.

CRediT authorship contribution statement

Zahra Khakpour: Project administration, Supervision.
Saeed Sedaghat: Writing – original draft, Investigation.
Mohammad Farvizi: Formal analysis, Conceptualization.
Nima Naderi: Methodology, Writing – review & editing.
Abouzar Massoudi: Data curation, Writing – review & editing.

Data availability

The data underlying this article will be shared on reasonable request to the corresponding author.

Declaration of competing interest

The authors declare no competing interests.

Declaration of AI use

The authors formally disclose the utilization of a Large Language Model (LLM), specifically a Gemini model developed by Google, for dedicated assistance in language editing, grammatical correction, and enhancing the manuscript's stylistic clarity. Subsequent to the AI's contribution, the authors performed a comprehensive, independent review and rigorous editing of the entire text, thereby accepting complete and exclusive responsibility for the scientific validity and overall accuracy of the final published content.

Funding and acknowledgment

This work was extracted from the master's thesis of the second author. The authors gratefully acknowledge the Materials and Energy Research Center (MERC) for providing the necessary materials and equipment. This research was supported under grant number RA-14-1-A.

References

[1] R. Tao, B. Steinhoff, K. Uzun, B. La Riviere, K. Sardo, et al., Correlation among porosity, mechanical properties, morphology, electronic conductivity and electrochemical kinetics of dry-processed electrodes, J. Power Sources. 581 (2023) 233481. https://doi.org/10.1016/j.jpowsour.2023.233481.

[2] A. Abedini, R. Shamskhani, A.A. Ebrahimi Valmoozi, S.S. Seyyed Afghahi, Effect of aging on corrosion and discharge performance of AZ63-1.5RE alloy as anode in magnesium-dissolved oxygen seawater batteries, J. Power Sources. 581 (2023) 233405. https://doi.org/10.1016/j.jpowsour.2023.233405.

[3] A. Caprì, A. Martínez-Lázaro, J. Béjar, I. Gatto, L. Álvarez-Contreras, et al., Three-dimensionally ordered macroporous trimetallic spinel for anion exchange membrane water electrolysis, Electrochim. Acta. 463 (2023) 142851. https://doi.org/10.1016/j.electacta.2023.142851.

[4] S. Kaenket, P. Suktha, K. Kongsawatvoragul, T. Sangsanit, P. Wuamprakhon, et al., Large-scale production of 18650 cylindrical supercapacitors: Effects of separators, electrode thickness, electrolyte additives, and testing protocols, J. Power Sources. 581 (2023) 233512. https://doi.org/10.1016/j.jpowsour.2023.233512.

[5] M. Rana, S. Ghosh, T. Nshizirungu, J.-H. Park, Catalytic depolymerization of Kraft lignin to high yield alkylated-phenols over CoMo/SBA-15 catalyst in supercritical ethanol, RSC Adv. 13 (2023) 30022–30039. https://doi.org/10.1039/D3RA05018A.

[6] Y. Xu, F. Wang, J. Wu, Y. Zhuang, D. Wu, et al., A difunctional interlayer of an activated carbon cloth supported with MoO2 catalyst for high-rate magnesium–sulfur batteries, J. Power Sources. 602 (2024) 234327. https://doi.org/10.1016/j.jpowsour.2024.234327.

[7] S.K. Pal, R. Saha, G.V. Kumar, S. Omar, Designing High Ionic Conducting NASICON-type Na3Zr2Si2PO12 Solid-Electrolytes for Na-Ion Batteries, J. Phys. Chem. C. 124 (2020) 9161–9169. https://doi.org/10.1021/acs.jpcc.0c00543.

[8] J. Kang, Z. Hu, M. Niu, J. Wang, Z. Qi, et al., Recent Advances in NASICON-Type Electrolytes for Solid-State Metal Batteries, Carbon Energy. e70031 (2025). https://doi.org/10.1002/cey2.70031.

[9] Z. Zhang, S. Wenzel, Y. Zhu, J. Sann, L. Shen, et al., Na3Zr2Si2PO12 : A Stable Na + -Ion Solid Electrolyte for Solid-State Batteries, ACS Appl. Energy Mater. 3 (2020) 7427–7437. https://doi.org/10.1021/acsaem.0c00820.

[10] H. Kim, J.H. Mason, W.K. Epting, H.W. Abernathy, A.D. Rollett, P.A. Salvador, Systematic and predictive trends to chromium poisoning in solid oxide fuel cell cathodes, J. Power Sources. 603 (2024) 234390. https://doi.org/10.1016/j.jpowsour.2024.234390.

[11] H.C. Prakash, M.S. Kumar, T.-W. Lin, S.K. Batabyal, Photo-assisted capacitive performance of V2O5 supercapacitor, Electrochim. Acta. 469 (2023) 143229. https://doi.org/10.1016/j.electacta.2023.143229.

[12] G. Nataliia, K. Veronika, Š. Petra, Influence of rare earth elements (REEs) on the structure and optical properties of lithium zirconium phosphate (LZP), CrystEngComm. 22 (2020) 5890–5899. https://doi.org/10.1039/D0CE00873G.

[13] L. Lin, K.B. Hatzell, Polymorphism control of fast-sintered NASICON-type LiZr2(PO4)3, J. Mater. Chem. A. 12 (2024) 29932–29940. https://doi.org/10.1039/D4TA04507F.

[14] A. Cassel, B. Fleutot, M. Courty, V. Viallet, M. Morcrette, Sol-gel synthesis and electrochemical properties extracted by phase inflection detection method of NASICON-type solid electrolytes LiZr2(PO4)3 and Li1.2Zr1.9Ca0.1(PO4)3, Solid State Ion. 309 (2017) 63–70. https://doi.org/10.1016/j.ssi.2017.07.009.

[15] S. Khatua, Y.B. Rao, K.R. Achary, L.N. Patro, Li-ion transport studies of NASICON-type LiZr2(PO4)3 solid electrolyte crystallizing in rhombohedral structure at room temperature, Surf. Interfaces. 41 (2023) 103212. https://doi.org/10.1016/j.surfin.2023.103212.

[16] Z. Khakpour, S. Sedaghat, M. Farvizi, N. Naderi, A. Massoudi, Synthesis, sintering and electrical properties of Li1+xGdxZr2-x(PO4)3 solid electrolytes for Li-ion batteries, Synth. Sinter. 5 (2025) 82–92. https://doi.org/10.53063/synsint.2025.51205.

[17] X. Pu, X. Cheng, R. Yang, Y. Lin, R. Yan, et al., The Structural Distortion Caused by Li-Site Modification Improves the Conductivity of LiZr2(PO4)3 Electrolytes for Potential Applications in Solid-State Batteries, Chem. Mater. (2025). https://doi.org/10.1021/acs.chemmater.5c02159.

[18] M. Catti, Lithium Location in NASICON-Type Li+ Conductors by Neutron Diffraction. I. Triclinic α′-LiZr2(PO4)3, Solid State Ion. 123 (1999) 173–180. https://doi.org/10.1016/S0167-2738(99)00089-2.

[19] F.W. Aston, The isotopic constitution and atomic weights of hafnium, thorium, rhodium, titanium, zirconium, calcium, gallium, silver, carbon, nickel, cadmium, iron and indium, Proc. R. Soc. London Ser. A - Math. Phys. Sci. 149 (1935) 396–405. https://doi.org/10.1098/rspa.1935.0070.

[20] V.M.S. Muthaiah, S. Mula, Effect of zirconium on thermal stability of nanocrystalline aluminium alloy prepared by mechanical alloying, J. Alloys Compd. 688 (2016) 571–580. https://doi.org/10.1016/j.jallcom.2016.07.038.

[21] B. Lehnert, M. Hult, G. Lutter, G. Marissens, S. Oberstedt, et al., Constraints on partial half-lives of 136Ce and 138Ce double electron captur, Phys. Rev. C. 105 (2022) 045801. https://doi.org/10.1103/PhysRevC.105.045801.

[22] Y. Ma, L. Zhou, K. Zhang, X. Gai, J. He, X. Zhang, Effects of Cerium Doping on the Mechanical Properties and Energy-Releasing Behavior of High-Entropy Alloys, Materials (Basel). 15 (2022) 7332. https://doi.org/10.3390/ma15207332.

[23] D. Demirskyi, H. Borodianska, D. Agrawal, A. Ragulya, Y. Sakka, O. Vasylkiv, Peculiarities of the neck growth process during initial stage of spark-plasma, microwave and conventional sintering of WC spheres, J. Alloys Compd. 523 (2012) 1–10. https://doi.org/10.1016/j.jallcom.2012.01.146.

[24] M.I. Kimpa, M.Z.H. Mayzan, J.A. Yabagi, M.M. Nmaya, K.U. Isah, M.A. Agam, Review on Material Synthesis and Characterization of Sodium (Na) Super-Ionic Conductor (NASICON), IOP Conf. Ser. Earth Environ. Sci. 140 (2018) 012156. https://doi.org/10.1088/1755-1315/140/1/012156.

[25] A. Jonderian, E. McCalla, The role of metal substitutions in the development of Li batteries, part II: solid electrolytes, Mater. Adv. 2 (2021) 2846–2875. https://doi.org/10.1039/D1MA00082A.